

TOMOGRAPHY OF THE REIONIZATION EPOCH WITH MULTIFREQUENCY CMB OBSERVATIONS

CARLOS HERNÁNDEZ-MONTEAGUDO,¹ LICIA VERDE,¹ AND RAUL JIMENEZ¹

Draft version July 6, 2018

ABSTRACT

We study the constraints that future multifrequency Cosmic Microwave Background (CMB) experiments will be able to set on the metal enrichment history of the Inter Galactic Medium at the epoch of reionisation. We forecast the signal to noise ratio for the detection of the signal introduced in the CMB by resonant scattering off metals at the end of the Dark Ages. We take into account systematics associated to inter-channel calibration, PSF reconstruction errors and inaccurate foreground removal. We develop an algorithm to optimally extract the signal generated by metals during reionisation and to remove accurately the contamination due to the thermal Sunyaev-Zel'dovich effect. Although demanding levels of foreground characterisation and control of systematics are required, they are very distinct from those encountered in HI-21cm studies and CMB polarization, and this fact encourages the study of resonant scattering off metals as an alternative way of conducting tomography of the reionisation epoch. An ACT-like experiment with optimistic assumptions on systematic effects, and looking at *clean* regions of the sky, can detect changes of 3-12% (95% c.l.) of the OIII abundance (with respect its solar value) in the redshift range $z \in [12, 22]$, for reionization redshift $z_{\text{re}} > 10$. However, for $z_{\text{re}} < 10$, it can only set upper limits on NII abundance increments of $\sim 60\%$ its solar value in the redshift range $z \in [5.5, 9]$, (95% c.l.). These constraints assume that inter-channel calibration is accurate down to one part in 10^4 , which constitutes the most critical technical requirement of this method, but still achievable with current technology.

Subject headings: cosmic microwave background – intergalactic medium – abundances

1. INTRODUCTION

The Cosmic Microwave Background (CMB) radiation constitutes one of today's most useful tools in cosmology. The properties of its brightness temperature fluctuations carry information not only of the young Universe in which they arise, but also of the evolving Universe that CMB photons encounter in their way to the observer. First and second generation CMB experiments like COBE (Bennett et al. 1994), Tenerife (Gutiérrez et al. 2000), Boomerang (de Bernardis et al. 1999), Maxima (Hanany et al. 2000) and WMAP (Spergel et al. 2003, 2006; Bennett et al. 2003; Hinshaw et al. 2003, 2006), aim to characterize the properties of the *intrinsic* temperature fluctuations, imprinted in the CMB during the epoch of Hydrogen recombination at $z \sim 1, 100$, (Sunyaev & Zeldovich 1970). Third generation CMB experiments, however, scan the small angular scales searching for *secondary* temperature fluctuations, introduced well after CMB photons decouple from matter during recombination. Among all secondary anisotropies, those induced by the thermal Sunyaev-Zel'dovich (tSZ) effect (Sunyaev & Zel'dovich (1980), caused by the distortion induced by hot electrons as they transfer energy to low energy CMB photons via Compton scattering) and the kinematic Sunyaev-Zel'dovich effect ((Sunyaev & Zeldovich 1972), caused by a Doppler kick induced by moving electrons via Thomson scattering) are of outmost importance.

Indeed, the fact that the tSZ effect is a *redshift-independent* signal generated in hot dense electron clouds makes the tSZ a powerful tool to measure the abundance of galaxy clusters at all redshifts, which by itself can provide information about the presence and nature of Dark Energy in our Universe,

(e.g., Haiman et al. (2001)). Third generation experiments like South Pole Telescope (SPT, Ruhl et al. (2004)), and the Atacama Cosmology Telescope (ACT, Fowler et al. (2005)) will scan the sky at millimeter frequencies in an attempt to characterise the mass and redshift distribution of galaxy clusters in our Universe.

Here, we exploit the exquisite sensitivity level and angular resolution of these forthcoming experiments to study the impact of metals on CMB temperature fluctuations. Metals are first produced by stars at the end of the Dark Ages and during reionization (for a review see, e.g., Barkana & Loeb (2001)), and, as shown in Basu et al. (2004), they provide some effective optical depth to CMB photons due to resonant transitions. Basu et al. (2004) (hereafter BHMS) showed that neutral species such as C, O and Si, together with ions like CII, OIII or NII should leave their imprint on the CMB temperature anisotropy by means of resonant scattering of CMB photons on some of their transitions. They found that the leading consequence of such scattering is a slight blurring of the original CMB anisotropies (by a factor $\tau_{\nu_{rs}}$, with $\tau_{\nu_{rs}}$ the optical depth of a resonant transition) in the temperature maps and thus a contribution to the power spectrum proportional to the primordial CMB power spectrum with constant of proportionality given by $\tau_{\nu_{rs}}$. Peculiar velocities of metals should introduce new anisotropies, which however should only be visible in the very large angular scales. BHMS demonstrated that, under *ideal* conditions, future multifrequency CMB experiments should be able to set strong constraints on the abundances of metals ($10^{-4} - 10^{-2}$ solar fraction) in the redshift range $z \in [1 - 50]$, opening a new exploration window on the end of the Dark Ages and the reionization history of our Universe.

In this paper we build upon the work of BHMS paying particular attention to realistic aspects such as cross-channel

¹ Department of Physics and Astronomy, University of Pennsylvania, 209 South 33rd St, Philadelphia, PA 19104; carloshm@astro.upenn.edu, lverde.raulj@physics.upenn.edu

calibration, point spread function (PSF) characterization and foreground contamination, aiming to assess their real impact on the sensitivity of future CMB experiments to metal enrichment history. We study what level of experimental systematic and knowledge of contaminants is required in order to achieve a given sensitivity threshold. Our approach is general, but we will focus on ACT’s specifications (e.g., instrumental noise level, angular resolution and sky coverage, beam reconstruction etc.). Assuming a very accurate PSF characterization and inter-channel calibration for this experiment, we forecast ACT’s sensitivity to the signal generated by metals and the constraints on reionization history that can be inferred from it. Current and future dust observations will help to correct for dust emission to significantly low levels in already relatively dust-clean sky areas. Also, because of the redshift-independent frequency dependence of the non-relativistic tSZ, an accurate subtraction this effect should be possible if more than two frequency channels are available. We find that the following specifications are required to extract the signal from a realistic survey: cross channel calibration error at or below the 10^{-4} level, PSF characterisation at 0.1–1% level, efficient foreground removal. Foreground and PSF characterisation requirements are realistically achievable with an ACT-like experiment. The required accuracy in cross-channel calibration can certainly be achieved with Fourier Spectrometers, (Partridge 1995; Halpern et al. 1995). Such an experiment will be able to set strong constraints on the reionization history; in particular it should detect the presence of newly formed OII at redshift $z \sim 14$ for metallicities of the inter-galactic medium above 3% the solar value, at the 95% confidence level. These constraints will provide a critical consistency check for estimates of the optical depth to reionization and constraints on reionization history obtained from CMB polarization measurements. In addition these finding will provide a direct test of our understanding of reionization and metal enrichment of the IGM.

Since the measurement of the metallicity abundance is sensitive to a redshift window determined by the central frequency and the bandwidth of the detector, multifrequency observations will provide a tomographic reconstruction of the epoch of re-ionization. This should motivate future experiments aiming to perform reionization tomography via CMB multifrequency observations. We offer guidance for these future experiments and quantify their technical requirements. In Section 2 we briefly review how the signal we are trying to measure arises and in Section 3 we build a realistic model of the total signal to be measured by experiments. In Sections 4 and 5 we compare the signal generated at reionization with contaminants, and suggest different methods to extract it. In Section 6 we make predictions for an ACT-like experiment: we build a realistic foreground model and compute and discuss the limits that can be imposed on the reionisation and enrichment history of the Universe. We conclude in Sec. 7 discussing our results and prospects for future and dedicated experiments.

2. CMB RESONANT SCATTERING ON METALS

Following BHMS here we review how the signal of metals arises. Let us assume that a CMB experiment is observing at a given frequency ν_{obs} and that CMB photons interact with a species X via a resonant transition of resonant frequency ν_{rs} . It is clear that the CMB experiment may be sensitive to such interaction only in the redshift range centered on $z_{rs} = \nu_{rs}/\nu_{obs} - 1$, with its width depending on the frequency response of the detectors². The resonant scattering of this species will generate an optical depth to CMB photons which can be computed to be (Sobolev 1946):

$$\tau_X(z) = f_{rs} \frac{\pi e^2}{m_e c} \frac{\lambda_{rs} n_X(z)}{H(z)}. \quad (1)$$

Here, n_X is the number density of the X species, f_{rs} is the absorption oscillator strength of the resonant transition, λ_{rs} its wavelength, $H(z)$ is the Hubble function, e and m_e are the electron charge and mass, respectively, c is the speed of light.

The effect of resonant scattering on CMB anisotropies can be more easily seen when considering a single Fourier k -mode of the CMB temperature fluctuations. Such mode can be expressed as an integral of various sources along the line of sight (Hu & Sugiyama 1994):

$$\Delta_T(k, \eta_0, \mu) = \int_0^{\eta_0} e^{ik\mu(\eta-\eta_0)} \left[\Lambda(\eta)(\Delta_{T0} - i\mu v_b) \dot{\phi} + \psi - ik\mu\psi \right]. \quad (2)$$

In this equation, written for the conformal Newtonian gauge, η denotes conformal time, $\Lambda(\eta) \equiv \dot{\tau}(\eta) \exp[-\tau(\eta)]$ is the visibility function and $\tau(\eta) \equiv \int_{\eta}^{\eta_0} d\eta' \dot{\tau}(\eta')$ is the optical depth to CMB photons. For Thomson scattering, $\dot{\tau} = a\sigma_T n_e$ with a the scale factor, n_e the electron number density and σ_T the Thomson cross section, Δ_{T0} accounts for the intrinsic temperature fluctuations, and v_b denotes the Fourier mode for baryon peculiar velocities; ϕ and ψ are the Fourier coefficients of the scalar perturbations of the metric.

As the CMB is being observed at a given frequency ν_{obs} , the opacity due to the resonant transition can be approximated by

$$\dot{\tau}_X = \tau_X \delta_D(\eta - \eta_{rs}), \quad (3)$$

where η_{rs} corresponds to z_{rs} , that is, the redshift at which observed CMB photons could interact with the species X via resonant scattering. When plugging this opacity into eq.(2), one obtains that original anisotropies have been blurred by a factor $e^{-\tau_X}$, and that new anisotropies have been generated at the same redshift:

$$\Delta_T(k, \eta_0, \mu) = e^{-\tau_X} \Delta_{T_{orig}}(k, \eta_{rs}, \mu) + \Delta_{T_{new}}(k, \eta_{rs}, \mu) \quad (4)$$

In the limit of $\tau_X \ll 1$ (low metal abundance), we can retain only linear terms in τ_X . Thus the change in the anisotropies ($\Delta_T - \Delta_{T_{orig}}$) reduces to a *blurring* factor ($-\tau_X \Delta_{T_{orig}}$) plus a new term proportional to v_b , which is important only in the large scales (see Appendix A of BHMS for details). On the sphere, the blurring term is $\Delta(\delta T/T_0) = -\tau_X(\delta T/T_0)_{CMB}$ and in multipole space, $\Delta a_{\ell m} = -\tau_X a_{\ell m}^{CMB}$. Small scale experiments will be only sensitive to the blurring term, which will may be confused with other components present in the map. We address this issue in the next 3 sections.

3. MODEL OF MEASURED TEMPERATURES

The fluctuations measured at each pixel location by a given channel will be, in general, a sum of different components, namely intrinsic CMB fluctuations, tSZ-induced temperature fluctuations, metal-induced temperature fluctuations (which

² The frequency bandwidth of the detectors is assumed to be much larger than the line thermal broadening

we aim to extract), galactic and extragalactic contaminants and instrumental noise. Hence, the signal received by channel j observing a frequency ν_j is modeled as:

$$\mathbf{T}_j = f_j \left[W_j * \left(\mathbf{T}_{CMB} + \mathbf{T}_{tSZ,j} + \sum_M \mathbf{T}_{M,j} + \sum_F \mathbf{T}_{F,j} \right) + \tilde{\mathbf{N}}_j \right], \quad (5)$$

where M stands for sum over *metals* and F for sum over *foregrounds*, $\tilde{\mathbf{N}}$ denotes instrumental noise, and all j indices refer to frequency ν_j ; f_j is an overall factor containing the calibration factor of the given channel, and W_j represents its beam or point spread function (hereafter PSF). The symbol $*$ denotes convolution. One can rewrite the Fourier counterpart of the previous equation as:

$$\tilde{a}_{\ell m}^j = f_j \left[W_{lm}^j \left(a_{\ell m}^{CMB} + g_{tSZ,j} a_{\ell m}^{tSZ} + \sum_M g_{M,j} a_{\ell m}^M + \sum_F g_{F,j} a_{\ell m}^F \right) + \tilde{N}_{lm}^j \right]. \quad (6)$$

This time we have split the peculiar frequency dependence of temperature fluctuations of tSZ ($g_{tSZ,j}$), foregrounds ($g_{F,j}$) and metals ($g_{M,j}$) from the multipole (ℓ) dependence (i.e. $g_{X,j} \equiv 1$ for a reference channel). However to keep track explicitly of the “real life effects”, we will work with the $a_{\ell m}^j$ ’s, defined as:

$$a_{\ell m}^j \equiv \frac{\tilde{a}_{\ell m}^j}{(W_{lm}^j)^{model}} = f_j \left[B_{\ell m}^j \left(a_{\ell m}^{CMB} + g_{tSZ,j} a_{\ell m}^{tSZ} + \sum_M g_{M,j} a_{\ell m}^M + \sum_F g_{F,j} a_{\ell m}^F \right) + N_{lm}^j \right]. \quad (7)$$

In this equation, $B_{\ell m}^j \equiv W_{lm}^j / (W_{lm}^j)^{model} = 1 + \epsilon_{\ell m}^j$ expresses the departure of the *real* PSF from the *model* PSF, (i.e. if the PSF is perfectly determined, $\epsilon_{\ell m}^j = 0$ and $B_{\ell m}^j = 1$). The noise has been redefined as $N_{lm}^j \equiv \tilde{N}_{lm}^j / (W_{lm}^j)^{model}$. Finally, if we set some frequency channel i to be the *reference* channel, we can write the calibration factor f_j as

$$f_j = 1 + \eta_j, \quad (8)$$

where η_j denotes the error in the relative calibration with respect to channel k . As working hypotheses, we shall assume that both calibration and PSF characterization are *very* accurate, i.e., $\eta^j \ll 1$ and $|\epsilon_{\ell m}^j| \ll 1$.

The signal induced by metals can be rewritten as

$$\sum_M g_{M,j} a_{\ell m}^M = -\tau_{\text{eff}}^j a_{\ell m}^{CMB}, \quad (9)$$

where the frequency dependence of the effective optical depth measures the amount of metals present in the redshift range probed by the observing frequency and the frequency of the resonant transition (rs), $z_{rs} = \nu_{rs} / \nu_{obs} - 1$. The lowest frequency channel will correspond to the highest redshift range, for which we will assume that the metal abundance is lowest, and therefore will be regarded as *reference* channel. We will attempt to measure *increments* of metal abundances with respect to such redshift by studying the difference map and the difference power spectra between different channels.

4. POWER SPECTRUM OF DIFFERENCE MAP VERSUS DIFFERENCE OF POWER SPECTRA

4.1. The difference map

The difference map between channels j and i in multipole space is,

$$\begin{aligned} \delta a_{\ell m}^{ji} \equiv a_{\ell m}^j - a_{\ell m}^i = \\ a_{\ell m}^{CMB} \left[f_j B_{\ell m}^j - f_i B_{\ell m}^i - (f_j B_{\ell m}^j \tau_{\text{eff}}^j - f_i B_{\ell m}^i \tau_{\text{eff}}^i) \right] + \\ a_{\ell m}^{tSZ} \left[f_j B_{\ell m}^j g_{tSZ,j} - f_i B_{\ell m}^i g_{tSZ,i} \right] + \sum_F a_{\ell m}^F \left[f_j B_{\ell m}^j g_{F,j} - f_i B_{\ell m}^i g_{F,i} \right] \\ + f_j N_{\ell m}^j - f_i N_{\ell m}^i. \end{aligned} \quad (10)$$

Since we assume accurate calibration and PSF characterization $f_j B_{\ell m}^j - f_i B_{\ell m}^i \simeq 2(\eta_j - \eta_i + \epsilon_{\ell m}^j - \epsilon_{\ell m}^i) \equiv 2(\delta f_{ji} + \delta \epsilon_{\ell m}^{ji})$ and $f_j B_{\ell m}^j g_{X,j} - f_i B_{\ell m}^i g_{X,i} \simeq g_{X,j} - g_{X,i}$ for any frequency-dependent component X . Hence, eq. (10) can be re-written as

$$\begin{aligned} \delta a_{\ell m}^{ji} \simeq a_{\ell m}^{CMB} \left[2(\delta f_{ji} + \delta \epsilon_{\ell m}^{ji}) - \delta \tau_{\text{eff}}^{ji} \right] + a_{\ell m}^{tSZ} \left[g_{tSZ,j} - g_{tSZ,i} \right] + \\ \sum_F a_{\ell m}^F \left[g_{F,j} - g_{F,i} \right] + f_j N_{\ell m}^j - f_i N_{\ell m}^i, \end{aligned} \quad (11)$$

with $\delta \tau_{\text{eff}}^{ji} \equiv \tau_{\text{eff}}^j - \tau_{\text{eff}}^i$.

This equation already shows the main limiting factor in our procedure: the accuracy of the cross-channel calibration. If δf_{ji} is negligible, then it should be possible to filter the $\delta a_{\ell m}^{ji}$ to recover $\delta \tau_{\text{eff}}^{ji}$ and discriminate it from the remaining signals, which should show, a priori, a *different* spatial pattern³. However, if δf_{ji} is non zero, then it will give rise to a spurious signal of identical spatial properties to the signal we are after ($-\delta \tau_{\text{eff}}^{ji} a_{\ell m}^{CMB}$), and hence indiscernible from it. Therefore, the calibration uncertainties set an unavoidable limit to the sensitivity of a CMB experiment that aims to measure the signal induced by scattering on metals during reionization.

4.2. Difference of power spectra versus power spectrum of difference map.

We next investigate the possibility of detecting the metal-induced signal in the power spectrum. There are two relevant quantities in this context: the difference of the power spectra computed at two different frequencies, $\delta C_l^{ji} \equiv C_l[\mathbf{T}_j] - C_l[\mathbf{T}_i]$ and the power spectrum of the difference map, $C_l[\mathbf{T}_j - \mathbf{T}_i]$. The latter consists on an average of $|\delta a_{\ell m}^{ji}|^2$, which, according to eq. (11), reads

$$\begin{aligned} |\delta a_{\ell m}^{ji}|^2 = |a_{\ell m}^{CMB}|^2 \left[|\delta f_{ji} + \delta \epsilon_{\ell m}^{ji}|^2 + (\delta \tau_{\text{eff}}^{ji})^2 - 2\delta \tau_{\text{eff}}^{ji} \mathcal{R}[\delta f_{ji} + \delta \epsilon_{\ell m}^{ji}] \right] \\ + |a_{\ell m}^{tSZ}|^2 (\Delta g_{tSZ}^{ji})^2 + \sum_F |a_{\ell m}^F|^2 (\Delta g_{F,F}^{ji})^2 \end{aligned}$$

³ We are assuming that errors in the PSF characterization are *uncorrelated* with the intrinsic CMB field, making the field $\delta \epsilon_{\ell m}^{ji} a_{\ell m}^{CMB}$ spatially independent of $a_{\ell m}^{CMB}$

$$\begin{aligned}
& + 2 \sum_{F_u > F_v} \mathcal{R}[a_{\ell m}^{F_u} (a_{\ell m}^{F_v})^*] \Delta g_{F_u}^{ji} \Delta g_{F_v}^{ji} + \mathcal{O}[\delta N_{\ell m}^2] \\
& + 2 \mathcal{R}[a_{\ell m}^{CMB} (\delta f_{ji} + \delta \epsilon_{\ell m}^{ji}) (a_{\ell m}^{tSZ})^*] \Delta g_{tSZ}^{ji} \\
& - 2 \mathcal{R}[a_{\ell m}^{CMB} (a_{\ell m}^{tSZ})^*] \delta \tau_{\text{eff}}^{ji} \Delta g_{tSZ}^{ji} \\
& + 2 \sum_F \mathcal{R}[a_{\ell m}^{CMB} (\delta f_{ji} + \delta \epsilon_{\ell m}^{ji}) (a_{\ell m}^F)^*] \Delta g_F^{ji} \\
& - 2 \sum_F \mathcal{R}[a_{\ell m}^{CMB} (a_{\ell m}^F)^*] \delta \tau_{\text{eff}}^{ji} \Delta g_F^{ji} \\
& + 2 \sum_F \mathcal{R}[a_{\ell m}^{tSZ} (a_{\ell m}^F)^*] \Delta g_{tSZ}^{ji} \Delta g_F^{ji} + \mathcal{O}[\text{cross terms } N_{\ell m}]. \tag{12}
\end{aligned}$$

For third generation CMB experiments, instrumental noise will not be a limiting factor, and therefore here we have neglected the cross terms where they appear. $\Delta g_X^{ji} \equiv g_{X,j} - g_{X,i}$ for any frequency dependent component X , and $\mathcal{R}[Y]$ denotes the real part of Y ; F_u and F_v denote different foreground components. This equation simplifies considerably under the assumption that $\delta f_{ji} + \delta \epsilon_{\ell m}^{ji}$ and $\delta \tau_{\text{eff}}^{ji}$ are much smaller than the typical amplitudes of tSZ and foregrounds. In this case, the average ($\sum_m / (2\ell + 1)$) of eq. (12) becomes:

$$\begin{aligned}
\langle |\delta a_{\ell m}^{ji}|^2 \rangle & \approx \langle |a_{\ell m}^{tSZ}|^2 \rangle \langle (\Delta g_{tSZ}^{ji})^2 \rangle + \sum_F \langle |a_{\ell m}^F|^2 \rangle \langle (\Delta g_{F,F}^{ji})^2 \rangle \\
& + 2 \sum_{F_u > F_v} \mathcal{R}[|a_{\ell m}^{F_u} (a_{\ell m}^{F_v})^*|] \Delta g_{F_u}^{ji} \Delta g_{F_v}^{ji} \tag{13}
\end{aligned}$$

The last term in eq. (12) has been neglected because the correlation between tSZ and foregrounds becomes negligible when massive cluster are excised from the maps (see sec. 6). That is, the power spectrum of the difference map provides a template for the dominant foregrounds in the case where the metal-induced signal is subdominant in $\mathbf{T}_j - \mathbf{T}_i$. We will show in Section (6.2) that the spatial properties of foregrounds inferred from this statistic can be used to optimize the search for signatures of reionization.

We next compute the difference of the power spectra computed at the channels considered, j and i . Noting that

$$\delta C_{\ell}^{ji} \equiv C_{\ell}[\mathbf{T}_j] - C_{\ell}[\mathbf{T}_i] = \frac{1}{2\ell+1} \sum_m \left(|a_{\ell m}^j|^2 - |a_{\ell m}^i|^2 \right), \tag{14}$$

a straightforward calculation for $|a_{\ell m}^j|^2 - |a_{\ell m}^i|^2$ yields

$$\begin{aligned}
|a_{\ell m}^j|^2 - |a_{\ell m}^i|^2 & \simeq 2 |a_{\ell m}^{CMB}|^2 \left(\mathcal{R}[\delta f_{ji} + \delta \epsilon_{\ell m}^{ji}] - \delta \tau_{\text{eff}}^{ji} \right) \\
& + |a_{\ell m}^{tSZ}|^2 \Delta[(g_{tSZ}^{ji})^2] + \sum_F |a_{\ell m}^F|^2 \Delta[(g_F^{ji})^2] \\
& + 2 \sum_{F_u > F_v} \mathcal{R}[a_{\ell m}^{F_u} (a_{\ell m}^{F_v})^*] \Delta[g_{F_u}^{ji} g_{F_v}^{ji}] \\
& + |N_j|^2 - |N_i|^2 + 2 \mathcal{R}[a_{\ell m}^{CMB} (a_{\ell m}^{tSZ})^*] \Delta[g_{tSZ}^{ji}] \\
& + 2 \sum_F \mathcal{R}[a_{\ell m}^{CMB} (a_{\ell m}^F)^*] \Delta[g_F^{ji}] + 2 \sum_F \mathcal{R}[a_{\ell m}^{tSZ} (a_{\ell m}^F)^*] \Delta[g_{CMB}^{ji} g_F^{ji}] \\
& + \mathcal{O}[(\delta \tau_{\text{eff}}^{ji})^2] + \mathcal{O}[\text{cross terms } \delta \tau_{\text{eff}}^{ji}] \tag{15}
\end{aligned}$$

The first term in the RHS of this equation reminds us of the importance of the calibration, since no signal will be measured if $\delta f^{ji} \sim \delta \tau_{\text{eff}}^{ji}$. The requirements on the amplitude of the PSF error $\delta \epsilon^{ji}$ are less strict than those of δf^{ji} , since its real part can flip sign and eventually will average to zero after combining different modes. Note that our signal is proportional to $\delta \tau_{\text{eff}}^{ji}$, and *not* to $(\delta \tau_{\text{eff}}^{ji})^2$, (Hernández-Monteagudo & Sunyaev 2005). Since our analysis is restricted to small ($\ell > 200$) scales, the correlation between the Integrated Sachs-Wolfe (ISW) component and the tSZ and extragalactic foregrounds can be neglected, because these signals are only relevant at large angles. Indeed, the tSZ and ISW correlation shows small ($\sim 3\text{--}1 \mu\text{K}$) amplitudes at $\ell > 300$, (Hernández-Monteagudo & Sunyaev 2005). The correlation between the tSZ and other foregrounds (e.g. radio galaxies) is also negligible once bright galaxy clusters are excised out. If we further neglect noise (as done in eq. 12 above), then we are left with

$$\begin{aligned}
\langle |a_{\ell m}^j|^2 - |a_{\ell m}^i|^2 \rangle & \approx 2 \langle |a_{\ell m}^{CMB}|^2 \rangle \left(\mathcal{R}[\langle \delta f_{ji} + \delta \epsilon_{\ell m}^{ji} \rangle] - \delta \tau_{\text{eff}}^{ji} \right) + \\
& \langle |a_{\ell m}^{tSZ}|^2 \rangle \Delta[(g_{tSZ}^{ji})^2] + \sum_F \langle |a_{\ell m}^F|^2 \rangle \Delta[(g_F^{ji})^2] \\
& + 2 \sum_{F_u > F_v} \langle \mathcal{R}[a_{\ell m}^{F_u} (a_{\ell m}^{F_v})^*] \rangle \Delta[g_{F_u}^{ji} g_{F_v}^{ji}] \tag{16}
\end{aligned}$$

If tSZ is the only significant contaminant in the maps, then the ℓ shape of its power spectrum can be obtained from the difference map power spectrum, eq.(11), and removed from $|a_{\ell m}^j|^2 - |a_{\ell m}^i|^2$. Note that this is only possible because the spectral dependence of the tSZ is known to high accuracy and bright clusters have been excised. In more adverse scenarios, eq.(11) should always provide a rough estimate of the amplitude and shape of the foreground power spectrum present in $|a_{\ell m}^j|^2 - |a_{\ell m}^i|^2$. Note that the signal we are searching for has a definite well known ℓ -pattern, identical to that of C_{ℓ}^{CMB} .

5. APPLYING A TEMPLATE FIT

Since we know what the spatial pattern of the signal we are trying to unveil is; $\mathbf{T}_{ji}[\hat{\mathbf{n}}] = -\delta \tau_{\text{eff}}^{ji} \mathbf{T}^{CMB}[\hat{\mathbf{n}}]$, with $\hat{\mathbf{n}}$ denoting a position on the sky, and we are aiming to measure one single parameter ($\delta \tau_{\text{eff}}^{ji}$), it is justified to write the following model for the measured difference map:

$$(\mathbf{T}_j - \mathbf{T}_i)[\hat{\mathbf{n}}] = \mathbf{N}[\hat{\mathbf{n}}] - \delta \tau_{\text{eff}}^{ji} \mathbf{T}^{CMB}[\hat{\mathbf{n}}], \tag{17}$$

where \mathbf{N} contains all the contaminating signals.

If we assume that the signal \mathbf{N} is gaussianly distributed⁴, then an optimal estimator for $\delta \tau_{\text{eff}}^{ji}$ is given by (Górski et al. 1996):

$$E[\delta \tau_{\text{eff}}^{ji}] = -\frac{(\mathbf{T}_j - \mathbf{T}_i)^t \mathbf{C}^{-1} \mathbf{T}^{CMB}}{(\mathbf{T}^{CMB})^t \mathbf{C}^{-1} \mathbf{T}^{CMB}}, \tag{18}$$

with \mathbf{C} the covariance matrix of \mathbf{N} (i.e. all the spurious signals regarded as noise), which is simply the Legendre transform of

⁴ If this is not the case, our matched filter of eq.(18) still provides an unbiased estimate of $\delta \tau_{\text{eff}}^{ji}$

eq.(11). The formal error associated to $E[\delta\tau_{\text{eff}}^{ji}]$ is then given by

$$\sigma_{\delta\tau_{\text{eff}}^{ji}}^2 = \frac{1}{(\mathbf{T}^{CMB})^t \mathbf{C}^{-1} \mathbf{T}^{CMB}}. \quad (19)$$

One must keep in mind, however, that the inversion of \mathbf{C} might not be trivial, since its dimensions are $N_{px} \times N_{px}$, with N_{px} the number of pixels of the map to be analyzed. If N_{px} is greater than a few thousands, the inversion of the covariance matrix poses numerical problems. We adopt the approach presented in Hernández-Monteagudo, Genova-Santos & Atrio-Barandela (2006) of dividing the map into different equal-sized patches for which the covariance matrix inversion is doable, and then combining the estimates of $\delta\tau_{\text{eff}}^{ji}$ obtained from each patch. Therefore, for each patch β , we obtain an estimate of the increment in optical depths $\delta\tau_{\text{eff}}^{ji,\beta}$ and an associated error $\sigma_{\delta\tau_{\text{eff}}^{ji,\beta}}$ given by

$$E[\delta\tau_{\text{eff}}^{ji,\beta}] = -\frac{(\mathbf{T}_{j,\beta} - \mathbf{T}_{i,\beta})^t (\mathbf{C}^{\beta,\beta})^{-1} \mathbf{T}_{\beta}^{CMB}}{(\mathbf{T}_{\beta}^{CMB})^t (\mathbf{C}^{\beta,\beta})^{-1} \mathbf{T}_{\beta}^{CMB}} \quad (20)$$

and

$$\sigma_{\delta\tau_{\text{eff}}^{ji,\beta}}^2 = \frac{1}{(\mathbf{T}_{\beta}^{CMB})^t (\mathbf{C}^{\beta,\beta})^{-1} \mathbf{T}_{\beta}^{CMB}}. \quad (21)$$

We combine the $\delta\tau_{\text{eff}}^{ji,\beta}$ estimates into a variance-weighted single estimate

$$E[\delta\tau_{\text{eff}}^{ji}] = \frac{\sum_{\beta} E[\delta\tau_{\text{eff}}^{ji,\beta}] / (\sigma_{\delta\tau_{\text{eff}}^{ji,\beta}})^2}{\sum_{\beta} 1 / (\sigma_{\delta\tau_{\text{eff}}^{ji,\beta}})^2}, \quad (22)$$

whose uncertainty takes into account the fact that estimates of $\delta\tau_{\text{eff}}^{ji,\beta}$ for *different* patches may not be independent:

$$\sigma_{\delta\tau_{\text{eff}}^{ji}}^2 = \frac{1}{\sum_{\beta} 1 / (\sigma_{\delta\tau_{\text{eff}}^{ji,\beta}})^2} \left[1 + 2 \times \frac{\sum_{\beta_1 < \beta_2} (\mathbf{T}_{\beta_1}^{CMB})^t (\mathbf{C}^{\beta_1,\beta_1})^{-1} \mathbf{C}^{\beta_1,\beta_2} (\mathbf{C}^{\beta_2,\beta_2})^{-1} \mathbf{T}_{\beta_2}^{CMB}}{\sum_{\beta} 1 / (\sigma_{\delta\tau_{\text{eff}}^{ji,\beta}})^2} \right]. \quad (23)$$

The second term in brackets vanishes if different patches are uncorrelated, i.e., $\mathbf{C}^{\beta_1,\beta_2} = 0$ for $\beta_1 \neq \beta_2$.

6. PROSPECTS FOR ACT

The Atacama Cosmology Telescope (ACT, Fowler et al. (2005)) will scan around 200 clean square degrees in the southern equatorial hemisphere in three frequency bands: 145 GHz, 220 GHz and 265 GHz. Its angular resolution and sensitivity levels (FWHM $\simeq 1'$, with $\sim 2\mu\text{K}$ of instrumental noise per pixel) have been optimized to study the tSZ effect in clusters of galaxies. Using these technical specifications we make predictions on the sensitivity of this experiment to the presence of metals at the end of the Dark Ages. We find that, beyond the strict requirements of cross-channel calibration and PSF characterization, the main limiting factor will be the presence of un-subtracted tSZ signal together with galactic dust emission. In what follows we will consider two cases, a pessimistic and an optimistic case, chosen to span the reasonable range of possibilities.

6.1. *Foreground model*

At the frequencies of ACT, we consider three main foreground contaminants: galactic dust, tSZ and infrared (IR) galaxies. Radio galaxies should contribute with sub-dominant contamination at these relatively high frequencies, and their spatial properties should be close to those of IR galaxies.

Dust: We build a model for dust emission based on the dust antenna temperature map provided by the WMAP team (Bennett et al. 2003) and available at the LAMBDA site⁵; this model was produced using the data of Finkbeiner et al. (1999). After converting it into thermodynamic temperature, we have computed its power spectrum outside foreground masks Kp0 and Kp2, (open triangles for Kp2, filled circles for Kp0 in Fig.1a), and fit it with power laws. This should provide a fair estimate of dust emission at ACT's frequencies. In reality however, dust cleaning of the actual data would need to be done directly on the maps. The maps have been scaled to ACT's frequencies by using the intensity spectral index given in Bennett et al. (2003) ($\alpha = 2.2 \pm 0.1$). Note that this is a conservative choice: this spectral index overpredicts the dust emission if compared to the shallower index ($\alpha \simeq 1.7$) measured by Ponthieu et al. (2005). We restrict our analyses to the *cleanest* third portion of the available sky in ACT's strip, for which the variance of dust-induced anisotropies is $\sim 4\%$ of the variance outside the Kp0 mask. Therefore, for our clean pixel subset we scale the dust power spectrum amplitude accordingly. We further assume that, after removing the existing dust model, the residuals vary from 10% (optimistic case) to 30% (pessimistic case) of the un-subtracted emission (in thermodynamic temperature). The dot-dashed line in Fig.(1c) shows the dust residuals in the power spectrum of the 265 GHz – 145 GHz difference map in the pessimistic case.

tSZ signal: The first step consists in removing all clearly detected sources. In practice this means that all pixels showing tSZ signals above the $\sim 4\sigma$ level should be excised; this excludes practically all clusters above $\sim 10^{14} M_{\odot}$ (see dotted line in Fig.1b). We are then left with the tSZ signal coming from smaller galaxy groups and the diffuse tSZ from a warm intergalactic gaseous component. When computing the power spectra of clusters and galaxy groups we consider both the Poisson term (C_{ℓ}^P , Atrio-Barandela & Mücke (1999)) and the correlation term (C_{ℓ}^C , Komatsu & Kitayama (1999))⁶. These terms are given by

$$C_{\ell}^P = \int dz \frac{dV(z)}{dz} \int_{M_{\min}}^{M_{\max}} dM \frac{dn}{dM} [M, z] |y_{\ell}(M, z)|^2 \quad (24)$$

and

$$C_{\ell}^C = \int dz \frac{dV(z)}{dz} P_m(k = \frac{\ell}{r(z)}, z) \times \left[\int_{M_{\min}}^{M_{\max}} dM \frac{dn}{dM} [M, z] b(M, z) y_{\ell}(M, z) \right]^2 \quad (25)$$

For galaxy groups we chose $M_{\min} = 5 \times 10^{12} M_{\odot}$ and $M_{\max} = 5 \times 10^{13} M_{\odot}$; $y_{\ell}(M, z)$ is the Fourier transform of the tSZ an-

⁵ LAMBDA URL site: <http://lambda.gsfc.nasa.gov>

⁶ The re-derivation of these terms in a line of sight approach (Hernández-Monteagudo et al. 2006) yielded expressions of smaller amplitude. Since the tSZ is regarded as a foreground, we conservatively use the equations given above.

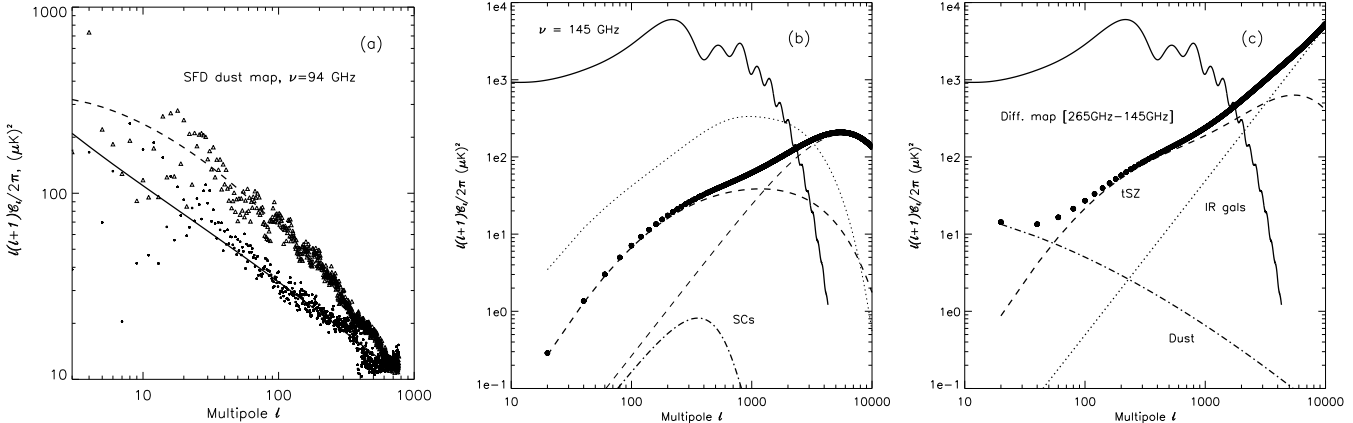


FIG. 1.— (a) Dust temperature power spectra as computed from the dust maps available at LAMBDA. Kp2 (empty triangles) and Kp0 (filled circles) masks have been applied, and the analytical fits used in our foreground forecast model. (b) tSZ signal present at 145 GHz. Once galaxy clusters above ACT’s 4- σ threshold have been removed (dotted line), only galaxy groups and diffuse gas in superclusters and filaments remain. The total tSZ residual (filled circles) is dominated by the galaxy group contributions, both from the Poissonian (thin dashed line) and the correlation (thick dashed line). The contribution of diffuse gas is negligible (dot-dashed line). (c) Power spectrum of the 265 GHz – 145 GHz difference map assuming no metal signal (filled circles), and its three components: tSZ (dashed line), IR sources (dotted line) and galactic dust (dot-dashed line).

gular profile of a cluster,

$$y(\hat{n}) = \int dr \sigma_T n_e \frac{k_B T_e}{m_e c^2}, \quad (26)$$

where σ_T is the Thomson cross-section, k_B the Boltzmann constant and T_e , m_e and n_e the electron temperature, mass and density, respectively; $b(M, z)$ is the bias factor of Mo & White (1996) relating the halo power spectrum to the underlying matter power spectra $P_m(k, z)$. Since we are interested in scales larger than the cluster, we took a gaussian profile for the gas distribution within these sources. Finally, we adopt a Press-Schechter mass function to characterise the mass and redshift distribution of collapsed objects. Since galaxy groups are smaller than galaxy clusters, the Poissonian term of the groups peaks at smaller angular scales than for clusters (see thin dashed line in Fig. (1b)). However, the distribution of galaxy groups is highly correlated, and this correlation dominates at large angles (thick dashed line in Fig. (1b)). These two terms are responsible for virtually all the tSZ residual signal present in the maps after subtracting the brightest galaxy clusters (solid circles). We associated diffuse gas into massive ($M > 10^{15} M_\odot$) structures that have turned around recently and hence still keep their linear size (superclusters). These structures are assumed to have an average overdensity of $\delta_{SC} \sim 20$ and a gas temperature of 0.2 KeV. These parameters should over-predict the diffuse tSZ signal and hence provide an upper limit; still this is negligible compared to the emission generated in galaxy groups. In Fig.(1b) the dot-dashed line gives the amplitude of the diffuse tSZ, which barely reaches the 1 μK level at sub-degree scales.

Infrared galaxies: Infrared galaxies present in ACT fields will be observed by BLAST⁷. Therefore, the major source of uncertainty should not be the amount of galaxies present within each ACT PSF, but how the measured flux at BLAST frequencies should be extrapolated at ACT frequencies. BLAST has three channels at 600 GHz, 860 GHz and 1200 GHz, and depending on the galaxy’s redshift these frequencies will probe the dust emission spectrum peak (high red-

shift) or the long wavelength tail (low redshift). To estimate flux of these sources at ACT lower frequencies, we need an estimate specific intensity spectral index α in the long wavelength tail, (i.e. $I_\nu \propto \nu^\alpha$ but α is expected to vary as a function of frequency).

We thus build the following model for the infrared galaxies foreground signal and its residuals. We use the results of Knox et al. (2004), which, based upon SCUBA⁸ observations, provides a spectral index of $\alpha_{SCUBA} = 2.6 \pm 0.3$ for the IR intensity over the range frequency 150-350 GHz. We use α_{SCUBA} to extrapolate IR source amplitudes from SCUBA to ACT frequencies. We assign BLAST sources an effective spectral index of $\alpha_{BLAST} \approx 2$ (shallower than that of SCUBA) to convert intensities between BLAST and ACT frequencies. This fixes our IR source model. We then introduce an error ($\delta\alpha_{BLAST}$) in the spectral index of 5% (optimistic case) and 20% (pessimistic case) of the model value of α_{BLAST} , and regard the subsequent error in extrapolated intensity as an estimate of residuals IR source subtraction. We neglect any type of spatial correlation of IR sources and hence the IR source residuals show a Poisson spectrum (see dotted line in Fig. 1c, which corresponds to $\delta\alpha_{BLAST}/\alpha_{BLAST} = 0.2$).

We see that infrared galaxies contaminate ACT maps at small scales, particularly at 265 GHz. This level of contamination can be lowered by excising out the brightest galaxies, but here we prefer to compute the forecasts without masking out more area. After all, at the angular scales at which the intrinsic CMB is dominant, the IR galaxy contribution is still below the tSZ residuals. Only at large angular scales the contribution from galactic dust is relevant. Fig. 1c shows our expectation for the power spectrum of the 265 GHz – 145 GHz difference map (filled circles), assuming that there is no metal-induced signal, together with its three components for our pessimistic case. This is the most contaminated scenario, as in the 220 GHz – 145 GHz difference map the dust and IR emission is remarkably smaller, and the tSZ signal is reduced since the non-relativistic tSZ brightness fluctuations vanish at

⁷ BLAST URL site: <http://chile1.physics.upenn.edu/blastpublic/index.shtml>

⁸ SCUBA URL site: <http://www.ifa.hawaii.edu/users/cowie/scuba/scuba.html>

218 GHz.

6.2. One step further: removing the tSZ

In Fig. 1c we see that the tSZ signal due to galaxy groups and small clusters is the main contaminant. Since for most of these sources the electronic temperature is such that relativistic corrections are negligible, it should be possible to exploit the known frequency dependence of the tSZ temperature fluctuations in order to remove them from the difference map. This is feasible if the CMB experiment has more than two frequencies, as it is the case for ACT.

For the sake of notation, let us refer to the 145 GHz, 220 GHz and 265 GHz channels of ACT as the i , j and k bands, respectively. Let m and n denote any arbitrary pair of ACT bands. The i channel is probing higher redshifts, and therefore will be used as the *reference* channel, so metal-induced optical depths in the j and k channel can be written as $\tau_{\text{eff}}^j = \tau_{\text{eff}}^i + \delta\tau_{\text{eff}}^{ji}$ and $\tau_{\text{eff}}^k = \tau_{\text{eff}}^i + \delta\tau_{\text{eff}}^{ki}$ respectively. Given any pair of ACT bands m and n , it is possible to build the following spatial template for tSZ signal:

$$\hat{\mathbf{S}}_{t\text{SZ}}^{mn} = \frac{\mathbf{T}_m - \mathbf{T}_n}{\Delta g_{t\text{SZ}}^{mn}}. \quad (27)$$

If the tSZ in band n is $\mathbf{T}_n^{t\text{SZ}} = g_{t\text{SZ},n} \mathbf{S}_{t\text{SZ}}$, then it is clear that $\hat{\mathbf{S}}_{t\text{SZ}}^{mn}$ will equal $\mathbf{S}_{t\text{SZ}}$ only if tSZ is the only component in the difference map, or dust and infrared emission, together with the metal-induced signature, are negligible. In such circumstances, the spatial power spectrum of this template should be equal to that given in eq.(13), and this step should provide a useful consistency check. Next we consider the difference map $\mathbf{T}_j - \mathbf{T}_i$. For this difference map, it is possible to remove two different tSZ templates, namely $\hat{\mathbf{S}}_{t\text{SZ}}^{ki}$ and $\hat{\mathbf{S}}_{t\text{SZ}}^{kj}$. That is:

$$\mathbf{R}_{ki}^{ji} = \mathbf{T}^j - \mathbf{T}^i - \Delta g_{t\text{SZ}}^{ji} \hat{\mathbf{S}}_{t\text{SZ}}^{ki}, \quad (28)$$

$$\mathbf{R}_{in}^{ji} = \mathbf{T}^j - \mathbf{T}^i - \Delta g_{t\text{SZ}}^{ji} \hat{\mathbf{S}}_{t\text{SZ}}^{kj}. \quad (29)$$

After introducing the dependencies on $\delta\tau_{\text{eff}}^{ji}$ and $\delta\tau_{\text{eff}}^{ki}$, the last equations become

$$\mathbf{R}_{kj}^{ji} = -\mathbf{T}^{CMB} \left[\delta\tau_{\text{eff}}^{ji} \left(1 - \frac{\Delta g_{t\text{SZ}}^{ji}}{\Delta g_{t\text{SZ}}^{ki}} \right) + \delta\tau_{\text{eff}}^{ki} \frac{\Delta g_{t\text{SZ}}^{ji}}{\Delta g_{t\text{SZ}}^{ki}} \right] + \delta\mathbf{R}_{kj}^{ji}, \quad (30)$$

$$\mathbf{R}_{ki}^{ji} = -\mathbf{T}^{CMB} \left[\delta\tau_{\text{eff}}^{ji} \left(1 - \frac{\Delta g_{t\text{SZ}}^{ji}}{\Delta g_{t\text{SZ}}^{ki}} \right) + \delta\tau_{\text{eff}}^{ki} \frac{\Delta g_{t\text{SZ}}^{ji}}{\Delta g_{t\text{SZ}}^{ki}} \right] + \delta\mathbf{R}_{in}^{ji}. \quad (31)$$

The equations for \mathbf{R}_{kj}^{ji} and \mathbf{R}_{ki}^{ji} constitute an equivalent system of equations (i.e. they no not add more information). The errors $\delta\mathbf{R}_{kj}^{ji}$ and $\delta\mathbf{R}_{ki}^{ji}$ contain residuals of the tSZ subtraction, together with linear combinations of dust and IR galaxy signals. From our foreground model, it is possible to estimate the covariance matrix of these errors. Further, if we apply a template fit introduced in the last part of Section (5) on \mathbf{R}_{mn}^{mi} and \mathbf{R}_{in}^{mi} , we obtain estimates of the quantities

$$\beta_{ki}^{ji} = \left[\delta\tau_{\text{eff}}^{ji} \left(1 - \frac{\Delta g_{t\text{SZ}}^{ji}}{\Delta g_{t\text{SZ}}^{ki}} \right) + \delta\tau_{\text{eff}}^{ki} \frac{\Delta g_{t\text{SZ}}^{ji}}{\Delta g_{t\text{SZ}}^{ki}} \right], \quad (32)$$

$$\beta_{in}^{mi} = \left[\delta\tau_{\text{eff}}^{ji} \left(1 - \frac{\Delta g_{t\text{SZ}}^{ji}}{\Delta g_{t\text{SZ}}^{ki}} \right) + \delta\tau_{\text{eff}}^{ki} \frac{\Delta g_{t\text{SZ}}^{ji}}{\Delta g_{t\text{SZ}}^{ki}} \right]. \quad (33)$$

Note these estimates for β_{ki}^{ji} and β_{in}^{mi} are computed over the same area on the sky, and the correlation between them arises due to the fact that foreground emission at different frequencies is correlated. This is also the cause for the correlation between $\delta\mathbf{R}_{ji}^{mi}$ and $\delta\mathbf{R}_{ki}^{ji}$, and for this reason we shall approximate the correlation coefficient matrix of β_{ki}^{ji} and β_{in}^{mi} by that of $\delta\mathbf{R}_{ji}^{mi}$ and $\delta\mathbf{R}_{ki}^{ji}$. Finally, we must recall that we are not interested on β_{ji}^{ji} or β_{ki}^{ji} , but on $\delta\tau_{\text{eff}}^{ji}$ and $\delta\tau_{\text{eff}}^{ki}$. The latter are just a linear transformations of the former, and this makes straightforward the transformation of the respective covariance matrices. It is clear that this procedure will be useful in case the tSZ component is far larger than the rest, since it removes most of the tSZ present in the difference maps at the expense of slightly increasing the level of the other contaminants.

6.3. Sensitivity on $\delta\tau_{\text{eff}}^{ji}$ and constraints on IGM enrichment

ACT will scan a strip of 2.5° width around the south celestial pole, at a constant declination of $\delta \simeq -55.3^\circ$. The resulting ring covering 400 square degrees will intersect the galaxy, and hence the clean area will be smaller and located at high galactic latitudes. In terms of dust emission, following the model of Finkbeiner et al. (1999), we select the ~ 140 cleanest square degrees, and group them into 83 patches of 500 pixels each. This will make us sensitive to changes in the power spectrum in a multipole range $\ell \in [80, 2000]$. We use the HEALPix⁹ (Górski et al. 2005) pixelization at resolution parameter $N_{\text{side}} = 1024$. The linear pixel size is close to 3.4 arcmins, and an effective convolution with a gaussian beam of FWHM = 4 arcmins is adopted for all components in all maps. We assume a PSF reconstruction uncertainty ranging from 0.2% (optimistic case) to 1% (pessimistic case) (i.e., $|\delta\epsilon_{\ell m}^{mn}| \sim 0.002 - 0.01 \forall l, m$) and consider how the cross-channel calibration error affects the constraints.

When computing the CMB power spectrum we use the cosmological parameters that best fit WMAP's first year data (Spergel et al. 2003), and as a CMB template (\mathbf{T}^{CMB}) we use one sky realization from such power spectrum. Foreground contamination is introduced according to subsection 6.1. In what follows, in the pessimistic case we assume PSF reconstruction error of 1%, dust emission residuals of 30% in the maps ($\sim 10\%$ in C_ℓ), 20% error in IR sources spectra index, no tSZ subtraction (after masking). In the optimistic case we assume $|\delta\epsilon_{\ell m}^{mn}| \sim 2 \times 10^{-3}$, 10% error in dust amplitude modeling, $\delta\alpha_{BLAST}/\alpha_{BLAST}$, of 5%, tSZ subtraction down to a 10% in the maps.

In Fig.(2a) we show the power spectra of the foreground residuals, for each of the two map differences, ji (or 265 - 145 GHz, solid lines) and ki (220 - 145 GHz, dashed lines). Thick lines correspond to the pessimistic case, thin lines to the optimistic case. We can see that the residuals power spectra become proportional to the CMB power spectra at $l \sim 200$, and that this fact is more visible when foreground subtraction is more accurate. This is due to the fact that PSF reconstruction errors $\delta\epsilon_{\ell m}^{ji}$ are taken to have, on average, the same amplitude for all multipoles ℓ 's. Hence $|\delta\epsilon_{\ell m}^{ji} a_{\ell m}^{CMB}|^2 \propto C_\ell^{CMB}$.

⁹ <http://healpix.jpl.nasa.gov>

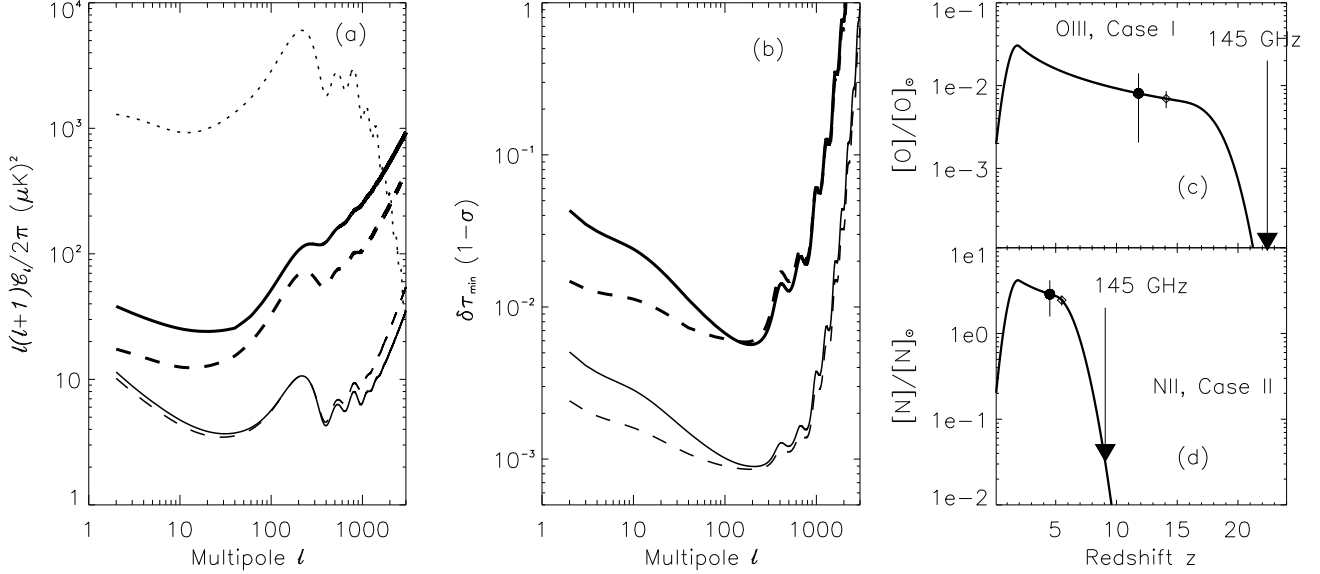


FIG. 2.— (a) Residual power spectra for the two map differences: 265 GHz - 145 GHz, (solid lines) and 220 GHz - 145 GHz (dashed lines). Thin lines correspond to the optimistic case, thick lines to the pessimistic case (see text for details). The dotted line shows the reference CMB power spectrum. (b) Minimum detectable $\delta\tau_{\text{eff}}^{\text{mn}}$ via a straight comparison of residual and CMB power spectra, i.e., $(\delta\tau_{\text{eff}}^{\text{mn}})_\ell = |C_\ell^{\text{res}}/(2 C_\ell^{\text{CMB}})|$, with C_ℓ^{res} the residual power as given in panel (a). (c) Constraints that ACT will be able to set if inter-channel calibration issues are not important. In a scenario with early ionization powered by massive Pop III UV emission, Oxygen will be twice ionized and ACT will be able to measure increments of its abundance of $\sim 3\%$ its solar value between redshifts 22 and 14, and increments of $\sim 12\%$ its solar value between redshifts 22 and 12. (d) In a late reionization scenario in which NII dominates the effective resonant scattering optical depth, ACT will detect increments in its abundance of $\sim 60\%$ its solar value between redshifts 9 and 5.5, and ~ 2.3 times its solar value between redshifts 9 and 4.5.

TABLE 1
SENSITIVITY ON $\delta\tau_{\text{eff}}^{\text{mn}}$

	Pessimistic case	Optimistic case
$\sigma_{\delta\tau_{\text{eff}}^{ji}}$	1.9×10^{-3}	2.2×10^{-4}
$\sigma_{\delta\tau_{\text{eff}}^{ki}}$	2.7×10^{-3}	3.0×10^{-4}

We forecast at what precision the $\delta\tau_{\text{eff}}^{\text{mn}}$ can be recovered via two different approaches. The first approach applies the template fit outlined in Section 5 on the residual level given by our pessimistic of foregrounds, whereas the second provides the sensitivity on $\delta\tau_{\text{eff}}^{\text{mn}}$ when the template fit is applied on the optimistic case. The errors on $\delta\tau_{\text{eff}}^{\text{mn}}$ are shown in Table 1 for the two map differences considered: ji (220 - 145 GHz) and ki (265 - 145 GHz). Note that the ratio $\delta C_\ell^{\text{mn}}/(2C_\ell^{\text{CMB}})$ can also provide a (less accurate) guess on $\delta\tau_{\text{eff}}^{\text{mn}}$. Finally, let us remark that these three ways of estimating the increment of the metal induced optical depth, although not independent, can provide useful mutual consistency checks. For experiments scanning larger areas (i.e., SPT), the errors in the template fit method would roughly scale like the inverse square root of the area covered.

The errors in Table 1 are given assuming that cross-channel calibration uncertainties are negligible. Thus if cross-channel calibration uncertainties (δf_{ji} , δf_{ki}) are worse than the values quoted in Table 1, then they will become the limiting factors in the measurements, (as already shown in eq.(11)). Since

abundances are proportional to optical depths (see eq.(1)), it follows that errors in abundances are proportional to cross-channel calibration errors in case the latter dominate over all other sources of errors. These levels are reachable with current Fourier Spectrometer technology, (Partridge 1995; Halpern et al. 1995).

If indeed inter-channel calibration is not an issue, then by comparing Table 1 with Table I in BHMS, we can infer that ACT will be able to set interesting constraints on the enrichment history. If Pop III stars ionized Oxygen twice, ACT will be able to detect increments of OIII abundances of $\sim 3\%$ its solar value between $z \sim 22$ and $z \sim 14$, and of $\sim 12\%$ its solar value between $z \sim 22$ and $z \sim 12$, at 95% confidence level, (see Fig. 2c). Note that these redshift ranges are particularly interesting, since they are close to the upper range for reionization redshift as indicated by WMAP ($z_{\text{re}} \simeq 11 \pm 2.5$ or $5 < z_{\text{re}} < 15$ at 2- σ level). Further, if reionization happens at the lower end of the WMAP values, and Nitrogen dominates the effective optical depth to CMB photons, then ACT will set constraints on the abundance of NII, since it can measure increments of $\sim 60\%$ its solar value between $z \sim 9$ and $z \sim 5.5$, and of ~ 2.3 times its solar value between $z \sim 9$ and $z \sim 4.5$, (95 % c.l., see Fig. 2d).

7. DISCUSSION AND CONCLUSIONS

The probability that a CMB photons is scattered by a given metal species depends primarily on two things: how abundant such species is and how likely the transition is. Indeed, as already shown in eq.(1), the Sobolev optical depth for the resonant transitions is proportional to the number density of ($n_i(z)$) the intervening species and the so-called oscillation strength of the transition (f_i). This means that for fixed metal

abundance, the oscillator strength, the transition wavelenght, and the relative population of the lower level involved in the transition will rule which lines are more *visible*. From Table 1 in BHMS, the transitions giving rise to higher optical depth correspond to OIII (88.36 μm , 51.81 μm), OI (63.18 μm), CII (157.74 μm) and NII (205.30 μm). For the frequency range of ground based experiments, O and N are the elements more likely to generate most of the optical depth to CMB photons. (Note that, although CII shows a strong transition, current Pop-III yield models predict low C/N abundance ratios, (Meynet, Ekström, & Maeder 2006)).

In the presence of only one species, say O, the technique presented here measures the increase of O abundance between some higher redshift bin (corresponding to the lowest frequency of the experiment) and lower redshift bins (corresponding to lower frequency bands). Under the additional assumption that the metal abundance at the highest redshift bin is negligible, the method yields constraint on the species abundance as a function redshift. In presence of different species (say O and N), this technique will be sensitive to the integrated effect of the different species. Note however that the same frequency band probes different redshift for resonant transitions of different elements. For example for OIII 145 GHz corresponds to $z \simeq 22$, 220 GHz to $z \simeq 14$ and 265 GHz to $z \simeq 12$, but for NII, 145 GHz corresponds to $z \simeq 9$, 220 GHz to $z \simeq 5.5$ and 265 GHz to $z \simeq 4.5$.

To interpret these measurements in light of the reionization process, we need a model of metal production for pop-III stars and an estimate of star formation rates at these redshifts. There have been recent advances in the computation of the yields for pop III stars (Meynet, Ekström, & Maeder 2006): a more careful modeling including the effect of rotation in the evolution of massive, low metallicity stars makes predictions for the properties of low metallicity halo stars in better agreement with observations. Star formation rate estimates are somehow dependent on the initial mass function, however the yields are relatively insensitive (Meynet, Ekström, & Maeder 2006) to the mass of the star for massive ($M > 10M_\odot$) stars and pop-III are expected to be massive (Abel et al. 2002). Therefore a constraint on the metal abundance obtained from measurements of the optical depth for resonant scattering, will translate into a constraint on the number of pop-III stars. Different reionization scenarios produce a different amount of pop-III stars as a function of redshift. While a detailed calculation along these lines will be presented elsewhere, we can show the potential impact of this technique and its complementarity with other probes of reionization with the following example. The nature of ionizing sources is not well understood (e.g. Barkana & Loeb (2001)). A detection of $\sim 12\%$ solar metallicity of oxygen at $z \sim 12$ would imply that pop-III stars played a major role in reionization and thus rule out the scenario of reionization by mini quasars.

In addition, the method presented here of tracing the reionization history with a measurement if the IGM enrichment, is complementary to other probes of reionization. For example the CMB is sensitive to ionizing photons produced during reionization and their escape fraction, and the horizon scale at reionization redshift. H 21 cm radiation probes neutral Hydrogen and the Ly- α forest has provided measurements of metallicities at $z \sim 4-5$. All these methods rely on different physics and thus provide a invaluable tool for understanding

the physics of reionization. In addition they are affected by foregrounds and systematics of very different nature, so their comparison provides a useful consistency check for the results.

The forecasts presented here are for an experiment designed with another goal in mind. It is interesting to ask how well an ideal experiment or a dedicated experiment could perform. A dedicated experiment would observe through the same PSF at different frequencies, in order to minimize the effects of PSF reconstruction errors. An self-calibrator device would assure accurate inter-channel calibration. The set of observing frequencies should be a compromise between accurate tSZ subtraction (this forces the ratios $g_{tSZ,i}/g_{tSZ,j}$, $g_{tSZ,i}/g_{tSZ,k}$ to be *far* from unity) and the choice of an interesting redshift range in terms of cosmic enrichment history (which is determined by transition frequencies of the metal species dominating the resonant scattering). Detector spectral widths verifying $\Delta\nu/\nu \gtrsim 0.1$ should assure that resonant scattering is dominant over collisional emission (see discussion in BHMS).

In our optimistic model for foregrounds, if the PSF reconstruction errors are smaller or equal than 5×10^{-4} , then foreground residuals are the limiting factors and the constraints on the abundances improve by a factor of three compared to the case considered here, for the same sky coverage. This sets the target for PSF reconstruction for a dedicated experiment. In this case the cross-cannel calibration requirements also becomes stricter by a factor four, achievable with current Fourier Spectrometer technology. Consider OIII and NII: the transitions quoted above (88.3 μm and 205.30 μm , respectively) will dominate the effective optical depth to CMB photons because of the pop III yields for these elements and because of the transition oscillator strength. For these elements, there is an optimal frequency range to probe reionization. The upper limit to the redshift of reionization sets the reference channel to be at $> 100\text{GHz}$. On the other end, at, say, 350 GHz, the level of contamination due to dust in the Galaxy and IR sources becomes important. We conclude that the optimal frequency window will be between 100 GHz and 350 GHz. This range fits well with the frequency coverage of Planck, and, at the same time, is well accessible by ground-based experiments.

In summary, we have presented an algorithm to realistically measure the signature of metals in the power spectrum of the CMB. We have shown how the different foregrounds can be removed and have presented a method to combine the maps at different frequencies optimally. The dominant foreground is the tSZ and the dominant source of error is the beam error and cross-channel calibration. We have forecasted the performance of the algorithm for an experiment with characteristics similar to ACT and have shown that one can constrain IGM abundances larger than 1% solar at $z > 10$. Since the method probes the metal abundance, and therefore the star formation rate, at the redshift corresponding to the frequency of the band, it is possible to do tomography of the metallicity enrichment process. Multifrequency CMB experiments can provide a tomographic reconstruction of the re-ionization epoch that is nicely complementary to other reionization probes.

ACKNOWLEDGMENTS

We thank Mark Devlin and Lyman Page for useful discussions on instrumentation and systematics control and Rashid A. Sunyaev for discussions that motivated this work and comments and criticism. Some of the results in this paper have been derived using the HEALPix¹⁰ (Górski et al. 2005) package. We acknowledge the use of the Legacy Archive for Microwave Background Data Analysis (LAMBDA). Support

for LAMBDA is provided by the NASA Office of Space Science. This research is supported in part by grant NSF AST-0408698 to the Atacama Cosmology Telescope. CHM and LV are supported by NASA grants ADP03-0000-0092 and ADP04-0000-0093. The work of RJ is supported by NSF grants AST0206031, AST-0408698, PIRE-0507768 and NASA grant NNG05GG01G.

¹⁰ HEALPix URL site: <http://healpix.jpl.nasa.gov>

REFERENCES

Abel, T., Bryan, G. L., & Norman, M. L. 2002, *Science*, 295, 93
 Atrio-Barandela, F. & Mücket, J. P. 1999, *ApJ*, 515, 465
 Barkana R., Loeb A., 2001, *PhR*, 349, 125
 Basu, K., Hernández-Monteagudo, C., & Sunyaev, R. A. 2004, *A&A*, 416, 447 [BHMS]
 Bennett, C. L., et al. 2003, *ApJS*, 148, 1
 Bennett, C.L. et al. 2003 *ApJS*, 148, 97
 Bennett, C. L., et al. 1994, *ApJ*, 436, 423
 de Bernardis, P., et al. 1999, *New Astronomy Review*, 43, 289
 Devlin, M. (private communication)
 Finkbeiner, D. P., Davis, M., & Schlegel, D. J. 1999, *ApJ*, 524, 867
 Fowler et al. 2005, astro-ph/0403137
 Górski, K. M., Banday, A. J., Bennett, C. L., Hinshaw, G., Kogut, A., Smoot, G. F., & Wright, E. L. 1996, *ApJL*, 464, L11
 Górski, K.M., E. Hivon, A.J. Banday, B.D. Wandelt, F.K. Hansen, M. Reinecke, & M. Bartelmann, 2005 *ApJ*, 622, 759
 Gutiérrez, C. M., Rebolo, R., Watson, R. A., Davies, R. D., Jones, A. W., & Lasenby, A. N. 2000, *ApJ*, 529, 47
 Haiman, Z., Mohr, J. J., & Holder, G. P. 2001, *ApJ*, 553, 545
 Halpern, M., Gush, H. P., Shinkoda, I., Tucker, G. S., & Towlson, W. 1995, *Astrophysical Letters Communications*, 32, 283
 Hanany, S., et al. 2000, *ApJL*, 545, L5
 Hernández-Monteagudo, C., Genova-Santos, R. & Atrio-Barandela, F. 2006, *ApJ*, (in preparation).
 Hernández-Monteagudo, C., & Sunyaev, R. A. 2005, *MNRAS*, 359, 597
 Hernández-Monteagudo, C., Verde, L., Jimenez, R. & Spergel, D. 2006, *ApJ*, (in press).
 Hinshaw, G., et al. 2003, *ApJS*, 148, 135
 Hinshaw, G., et al. 2006, ArXiv Astrophysics e-prints, arXiv:astro-ph/0603451
 Hu, W. & Sugiyama, N. 1994, *Phys. Rev. D*, 50, 627
 Knox, L., Holder, G. P., & Church, S. E. 2004, *ApJ*, 612, 96
 Komatsu, E., & Kitayama, T. 1999, *ApJL*, 526, L1
 Komatsu, E., & Seljak, U. 2001, *MNRAS*, 327, 1353
 Kosowsky A., 2003, *New Astron. Rev.* 47, 939
 Meynet G., Ekström S., Maeder A., 2006, *A&A*, 447, 623
 Mo, H. J., & White, S. D. M. 1996, *MNRAS*, 282, 347
 Partridge, R.B., *3K: the Cosmic Microwave Background Radiation*, 1995, Cambridge University Press, Cambridge
 Ponthieu, N., et al. 2005, *A&A*, 444, 327
 Ruhl, J., et al. 2004, *SPIE*, 5498, 11
 Sobolev, V.V. 1946, *Moving Atmospheres of Stars* (Leningrad: Leningrad State Univ.; English transl. 1960, Cambridge: Harvard Univ. Press)
 Spergel D. N., et al. 2003, *ApJS*, 148, 175
 Spergel, D. N., et al. 2006, ArXiv Astrophysics e-prints, arXiv:astro-ph/0603449
 Sunyaev, R. A., & Zeldovich, Y. B. 1972, *Comments on Astrophysics and Space Physics*, 4, 173
 Sunyaev, R. A. & Zel'dovich, I. B. 1980, *ARA&A*, 18, 537
 Sunyaev, R. A., & Zeldovich, Y. B. 1970, *ApJSS*, 7, 3